

Article

Deep Mineral Exploration of the Jinchuan Cu–Ni Sulfide Deposit Based on Aeromagnetic, Gravity, and CSAMT Methods

Jianmin Zhang ^{1,2}, Zhaofa Zeng ^{1,2,*}, Xueyu Zhao ^{1,2} , Jing Li ^{1,2,*}, Yue Zhou ^{1,2} and Mingxu Gong ^{1,2}

¹ College of Geo-Exploration Science and Technology, Jilin University, Changchun 130026, China; zjm16@mails.jlu.edu.cn (J.Z.); zhaoxueyu035035@163.com (X.Z.); zhouyue17@mails.jlu.edu.cn (Y.Z.); gongmx18@mails.jlu.edu.cn (M.G.)

² Key Laboratory of Applied Geophysics, Ministry of Natural Resources of PRC, Changchun 130026, China

* Correspondence: zengzf@jlu.edu.cn (Z.Z.); inter.lijing@gmail.com (J.L.)

Received: 31 December 2019; Accepted: 11 February 2020; Published: 13 February 2020



Abstract: The exploration of deep mineral resources is an important prerequisite for meeting the continuous demand of resources. The geophysical method is one of the most effective means of exploring the deep mineral resources with a large depth and a high resolution. Based on the study of the geological background, petrophysical properties, and aeromagnetic anomaly characteristics of the Jinchuan Cu–Ni sulfide deposit, which is famous throughout the world, this paper uses the widely used gravity, aeromagnetic, and CSAMT (controlled source audio-frequency magnetotellurics) methods with a complementary resolution to reveal the favorable prospecting position. In order to obtain better inversion results, the SL0 norm tight support focusing regularization inversion method is introduced to process the section gravity and aeromagnetic data of the mining area. By combining the results with CSAMT, it is found that the medium-low resistivity, high density, and the high magnetic anomaly areas near the structural belt can nicely correspond with the known ore-bearing rock masses in the mining area. At the same time, according to the geophysical exploration model and geological and physical property data, four favorable ore-forming prospect areas are delineated in the deep part of the known mining area.

Keywords: Jinchuan Cu–Ni sulfide deposit; deep mineral exploration; CSAMT; inversion

1. Introduction

Mineral resources are the material basis of human science and technology progress and social and economic development [1]. In recent years, with the continuous and stable growth of China's economy, the contradiction between the supply and demand of mineral resources has become increasingly prominent, among which all kinds of metal mineral resources are in short supply. The effective way to alleviate the shortage of resource supply is to carry out deep prospecting and strengthen the resource reserve. The Jinchuan Cu–Ni sulfide deposit is one of the three largest Ni–Cu–(PGE) deposits in the world. It is of great significance to carry out deep prospecting in this area to ensure the supply of copper and nickel resources. Moreover, the available geological data show that the deep parts of the known mining area and the surrounding area have a good prospecting potential, mainly based on the following: according to the metallogenic model, structural characteristics, and the spatial location of ore-bearing magma emplacement, there may be more ore bodies in the deep part of the mining area; the lower end of the main rock mass in the first, second, and third mining areas is not completely revealed; the new ore body is indeed found in the deep of the II mining area [2]. An independent ore body has been found in the surrounding rock at the bottom of No.24 ore body, with an increase of more

than 600,000 tons of nickel metal. It is believed that there may be a relatively rich copper–nickel sulfide ore bodies in the surrounding rocks in the footwall direction of the western rock bodies of Jinchuan, and there may be a large number of sulfide residues in the deep magma chamber corresponding to the eastern rock body [3]. For the surrounding area of the mining area, the previous data show that the rock mass of the mining area shows the characteristics of echelon arrangement in space, and there are new ore-bearing rock masses near the main ore body, such as No. 58 ore body of the third mining area [4].

The deep prospecting methods mainly include geological, geophysical, geochemical, and drilling methods. The geological prospecting method relies on the observation and analysis of surface outcrop or drilling core to infer the underground geological conditions, which has limitations for deep prospecting, especially for the concealed characteristics. Geochemical exploration is an important technical support condition for deep prospecting, and drilling engineering is the realization condition. However, the depth and scope that these two methods can reach is also limited. Geophysical exploration is the basic means to obtain the information of concealed parts beyond other prospecting methods, which has a large detection depth, a high resolution, and various means [5–8]. It can carry out multi-scale detection in the target area and provide rich information for deep ore prospecting [9,10]. Kheyrollahi et al. [11] discovered and predicted the distribution pattern of porphyry copper deposits in the tertiary magmatic belt by the upward extension and boundary enhancement of magnetic anomalies. Xiao and Wang [12] used Bouguer gravity and aeromagnetic data to further understand the geological and mineral resources near the porphyry copper molybdenum polymetallic mineralization in the Tianshan area of China. Hu et al. [13] explored potential iron and polymetallic lead–zinc–copper deposits in the Longmen area by the CSAMT method and found high-grade lead–zinc–silver–titanium ore through drilling based on inversion results. Guo et al. [14] applied the CSAMT method to the exploration of the Jianshui lead–zinc mine and drew the underground resistivity distribution map through data processing and inversion. According to the CSAMT results, the location of the ore body is inferred, and the results are verified by drilling. The lead–zinc ore body is 373.70–407.35 m in the well. Shah et al. [15] comprehensively used aeromagnetic induced polarization, magnetotelluric and borehole geological alteration, magnetic susceptibility, and density data to explore the copper–gold molybdenum Pebble porphyry deposit, and achieved good prospecting results. In order to accurately detect the underground structure of complex deposits and solve the problems of uniqueness and inconsistency in the single parameter inversion model, Zhang and Li [16] proposed a two-dimensional gravity gradient and a magnetotelluric joint inversion method based on data space and normalized cross gradient constraints. Melo et al. [17] proposed a geological characterization method that can identify copper deposits based on geophysical inversion. This method can use geophysical data and sparse geological information to evaluate the target quickly, especially for the first stage of deep target or concealed target exploration. The success of this method is verified by the inversion of magnetic data and the direct current resistivity data of Cristalino iron oxide copper gold deposit in northern Brazil. Lee et al. [18] obtained the resistivity model consistent with the regional geology through the 3D joint inversion of magnetotelluric and Z-axis tipper electromagnetic data, which not only shows the mineralization belt interpreted for the Morrison porphyry Cu–Au–Mo deposit but is also conducive to the exploration of the disseminated sulfide of other porphyry deposits.

Some researchers also used geophysical methods to carry out prospecting work in the Jinchuan copper–nickel mining area and its surrounding areas and obtained some knowledge or achievements. Through the joint interpretation of gravity and magnetic data, it is considered that the M-15 anomaly is caused by ultrabasic rocks with a buried depth of more than 1200 m, which has a positive effect on the indication of deep Cu–Ni deposits [19]. According to the comprehensive prospecting model of geology, geophysics, and geochemistry, Wen and Luo [20] carried out prospecting and prediction work in the deep and edges of the Jinchuan copper–nickel mining area and found five potential target areas. In 2006, Fu and Li [21] established a comprehensive geological geophysical prospecting model based on the characteristics of the geophysical geochemical field of rock masses and ore deposits in

different mining areas. On the basis of a systematic analysis of metallogenic geological conditions and comprehensive geophysical, geochemical, and remote sensing information, Gao [2] believed that the joint area of the first and second mining areas, the joint area of the I and II mining areas, the joint area of No.1 and No.2 ore bodies in the II mining area, and the overlap areas of geophysical and geochemical anomalies in the III mining area are important locations for ore body tracing.

On the basis of systematically summarizing the geological background of mineralization, this paper uses the aeromagnetic and gravity methods with low exploration cost and high efficiency, and the CSAMT method with a large exploration depth and a high vertical resolution to indicate the favorable metallogenic locations in the deep of the Jinchuan Cu–Ni deposit and its surrounding area. In order to overcome the weakness of deep signal in deep gravity and magnetic exploration, the processing method of potential field data is studied. Additionally, the focus inversion method based on the SL0 norm with a good convergence effect is used to process the aeromagnetic or gravity data of the profile, and, based on these results and the CSAMT inversion results, geological and physical properties data and geophysical profile data are interpreted. The results show that the range of the abnormal bodies corresponds well with the ore-bearing bodies of the known mining areas, and four favorable metallogenic targets are delineated according to the results.

2. Geological Background of the Survey Area

The Jinchuan Cu–Ni sulfide deposit is a part of the Longshoushan metallogenic belt, which is located in Longshoushan terrane in the southwest of the Alxa block of the North China Craton (NCC) [22,23]. The NCC is one of the three major Precambrian blocks in China, which formed from an amalgamation of micro blocks [24–26]. The Alxa block is located in the westernmost part of the NCC and is in fault contact with the Tarim craton to the west, bounded by the North Qilian orogenic belt in the south and the Central Asia orogenic belt in the north (Figure 1a) [27,28]. The Longshoushan terrane is a long narrow northwest trending uplift. It is 195 km long and 30–35 km wide, which is controlled by deep faults on both sides of the north and the south (F_1 and F_2). Its north side is adjacent to the Chaoshui basin, and its south side is separated from the Qilian orogenic belt (Figure 1b). In the Longshoushan terrane, the main outcropping strata are the Paleoproterozoic Longshoushan group, the late Mesoproterozoic Dunzigou group [29], and the Neoproterozoic–Cambrian Hanmushan group [30,31]. The Longshoushan group is the oldest metamorphic basement in the Longshoushan terrane [32]. Strong metamorphism and deformation in multiple periods [33] make the strata fragmented and it is difficult to judge the original stratigraphic sequence [34]. It mainly consists of schlieren and homogenic migmatites, marble, biotite-plagioclase gneiss, granulites, quartz schist, amphibolite, and pyroclastic rock [27,35]. The Dunzigou group is the earliest sedimentary overlying strata in the Longshoushan terrane, which is in angular unconformity contact with the lower Longshoushan group. In the geological history, the Longshoushan terrane has experienced multiple structural changes. The present NW trending faults and folds are mainly Caledonian and later structures. Faults in the Longshoushan terrane are mainly NW- and NE-trending structures, cutting the metamorphic formation [23]. Magmatic rocks are widely developed in the region, and magmatism occurred from Paleoproterozoic to Neoproterozoic, mainly in the Paleoproterozoic and the Paleozoic [36–39]. With regard to the formation age of Jinchuan intrusion, different researchers have adopted different methods to obtain a large number of isotopic age data, which can be roughly divided into two ranges: 1400–1600 Ma and 800–1000 Ma, representing Mesoproterozoic and Neoproterozoic, respectively [40,41].

The ore bearing ultrabasic rock bodies unconformity intrudes into the Baijiazuizi formation of pre-Great Wall system, which is in direct contact with gneiss, marble and banded migmatite, in the form of wall. It is about 6500 m long, 20–527 m wide on the surface (Figure 2a) and has a southwestern downward extension of more than 1000 m from the ground surface (Figure 2b) [28]. The overall strike is $N50^\circ W$, inclined to the SW, with a dip angle of 50° – 80° . The rock mass area is about 1.34 km². The ultramafic intrusion is divided into four sections by F_8 , F_{16-1} , and F_{23} and is numbered as III, I, II, and IV from west to east (Figure 2a), which are corresponding to the four mining areas, respectively.

The three main ore bodies with proved reserves of great economic value are respectively hosted in No.1 and No.2 ore bodies of Segment II and No.24 ore body of Segment I, and No.58 ore body is hosted in an independent rock body in the southwest side of Segment III (Figure 2b).

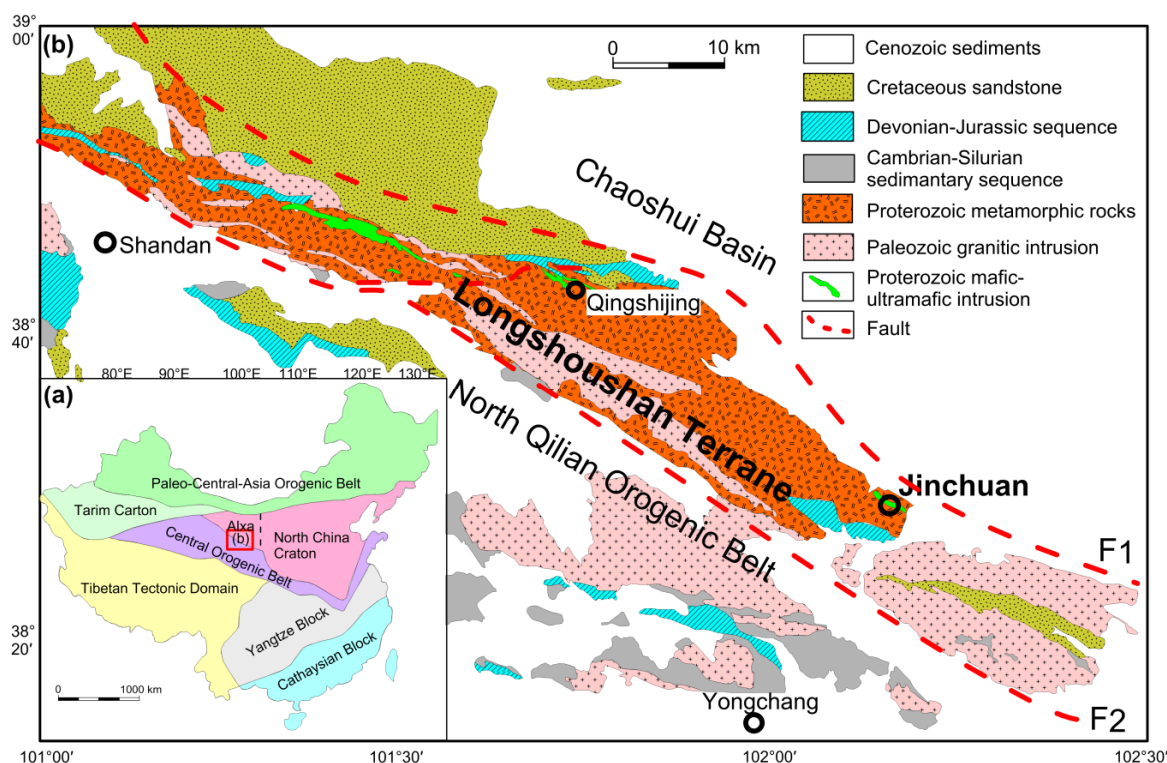


Figure 1. (a) The location of the study area and (b) a simplified geological map of the Longshoushan terrane. Both subfigures are based on [27,28].

The main strata in the mining area are the Baijiazuizi formation and the Quaternary system of the Longshoushan group of the pre-Great Wall system. The Quaternary sediments are mainly distributed in the east and west ends of the Jinchuan intrusion and the north of F₁. Baijiazuizi formation is the direct surrounding rock of the Jinchuan deposit, which is distributed in a NW–SE direction, consistent with the regional structural direction. Baijiazuizi formation underwent multiple magmatic intrusions and multiple metamorphisms, forming a series of rocks mainly composed of migmatite, gneiss, and marble (Figure 2a) [42]. Among them, gneiss with stable chemical properties and poor water permeability is a good barrier layer, which enables the ore-forming materials to fully crystallize and differentiate in ultrabasic magma. Marble is active in chemical properties. It is favorable for the formation of contact metasomatic mineralization [43]. Therefore, Baijiazuizi formation is an important prospecting indicator.

The mining area has experienced structural activities many times. The structures of different periods and different directions superposed each other, making the mining area fold and fracture developed. The axial near the EW fold group includes the anticline where the deposit is located and a large syncline in the south of the mining area. The axial near the NE fold group is nearly vertical to the NW direction main structural lines of the mining area, among which the NE direction fold group across the ultramafic rock mass is the most significant, which plays an important role in the shape change and mineralization re-enrichment of the ore body, and the rich ore body is obviously thickened at the turning part of the fold. The NW trending faults are the most developed, followed by the NE and nearly EW trending faults. As one of the most important ore-controlling factors, faults not only control the emplacement of an ore bearing rock but also control the re-enrichment of mineralization and the spatial position of ore body. The NW ore-controlling faults are related to the spatial distribution of ore

bodies. The NE or near EW ore controlling faults mainly cut the rock and ore bodies. The intersecting parts of faults in different directions can form irregular columnar ore bodies.

The ore-forming materials in the mining area mainly come from ultrabasic magma. Ultrabasic rock is the ore-forming parent rock and the surrounding rock of the main ore body. The relationship between ultrabasic rock and mineralization is mainly reflected in the spatial change of rock mass and the relationship between lithofacies and mineralization. Only the spatial relationship between the two is introduced here. The shape of ore-bearing rock mass is irregular, and the development of the ore body is closely related to the floor. Generally, the concave part of the floor is favorable for the accumulation of ore-forming materials, and the ore body is thick. The occurrence of ore-bearing rock mass controls the occurrence of the stratoid ore body, the ore body is the same as the rock mass, and the strike is NW. The thickness of the ore-bearing rock mass is related to the thickness of the rich ore body. At the bottom of the thick rock mass, the rich ore body is also thick, which can be seen in the first and second mining areas.

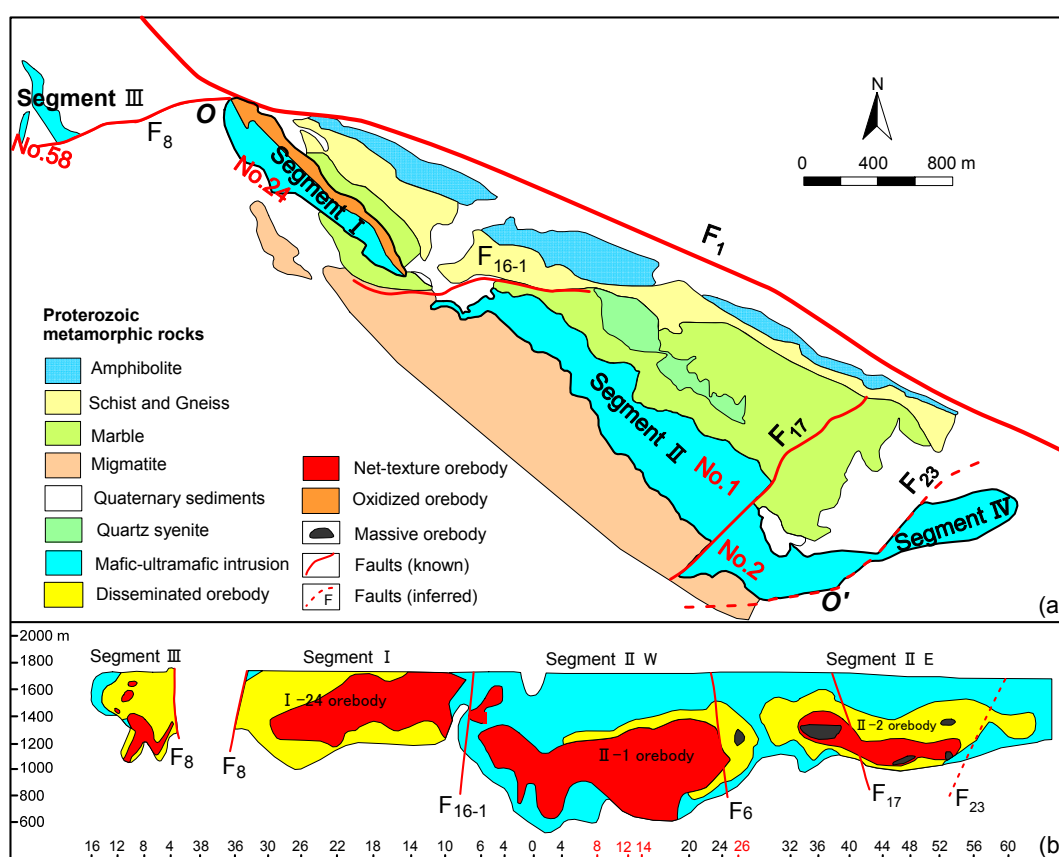


Figure 2. Geological map (a) and a cross section (b) of the Jinchuan intrusion, both subfigures are based on [28,42].

3. Aeromagnetic, Gravity, and CSAMT Surveys

Based on the characteristics of density, magnetism, and resistivity (Table 1), the rocks and ores in the mining area can be roughly divided into three categories. The first category is copper–nickel ore, showing the characteristics of high density, high magnetism, and low resistivity; the second category is ultrabasic rock, showing the characteristics of high density, strong magnetism, and medium resistivity; the third category is the rock surrounding the ultrabasic rock, with the characteristics of low density, weak magnetism, and high resistivity. The differences of these physical properties provide a precondition for geophysical exploration work such as gravity, magnetic, and electrical methods in the study area [21].

Table 1. Petrophysical properties in the Jinchuan Cu–Ni sulfide deposit [43], J_r represents remanent magnetization.

Rocks	Susceptibility (k)/ $4\pi \times 10^{-6}$ SI	$J_r/10^{-3}$ A·m ⁻¹	Density (σ)/ 10^3 kg·m ⁻³	Resistivity(ρ)/ Ω ·m
	Regular Value	Regular Value	Regular Value	Regular Value
Lherzolite	3900	900	2.72	320
Peridotite	2300	600	2.72	300
Migmatite	600	200		200
Granite	0	0	2.54~2.90	700
Gneissic granite	400	100	2.5	600
Biotite gneiss	0	0		
Marble	0	0	2.6	500
Amphibolite	200	200		376–1501
Tiny spotted ores	4300	800	2.73	62
Spotted ores	6100	500		90
Spongy ores	6600	1900	2.92	20

Convenient and efficient aeromagnetic exploration has been carried out in the main mining area. The aeromagnetic work uses the power glider as the carrier, and the measuring instrument is the helium optical-pumping magnetometer with a sensitivity of 0.001 nT. The average flight height is 93 m, the measurement scale is 1:10,000, the distance between survey lines is 100 m, and the distance between points is 2.7–3 m. The maximum dynamic noise level of the survey line in the survey area is 0.052 nT, most of which is less than 0.04 nT, and the average value is 0.027 nT, meeting the measurement requirements. Reduction to the pole can eliminate the asymmetry of the magnetic anomaly position caused by the declination and inclination of the magnetization field. After reducing magnetic anomaly to the pole, the anomaly information is more abundant, including the anomalies of different properties, scales, and depths. It is the basic data for anomaly interpretation. The induced magnetization of ultrabasic rocks and ores with high magnetic susceptibility in the Jinchuan Cu–Ni mining area is obviously greater than the residual magnetization [19], so reduction to the pole can be carried out, and the result is shown in Figure 3. The negative aeromagnetic anomaly of the mining area is located in the northeast, the isoline is relatively disordered, and the minimum negative anomaly is less than -140 nT. The positive aeromagnetic anomaly is mainly located in the southwest and central part, showing a significant northwest distribution. The known mining areas III, I, II, and IV (magenta curve range in Figure 3) are all in the high positive aeromagnetic anomaly area. The high positive anomaly in the III mining area is nearly circular, with a diameter of about 750 m, an area of about 0.4 km², and a maximum anomaly intensity of more than 350 nT. The high positive anomaly in the I mining area extends northwestward in a belt, with a length of about 1400 m, a width of about 600 m, and an area of about 0.75 km². The maximum anomaly value is located in the southeast end of the mining area, and the maximum anomaly value is more than 600 nT. The two ends of the high normal abnormal morphology in the II mining area have obvious distortion, but generally it is a strip extending northwestward, with a length of about 3000 m, a width of about 900 m in the west section, a width of about 650 m in the east section, an area of about 2.23 km², and the maximum abnormal value is more than 1500 nT. In addition, the cascade zones on both sides of the I and II mining areas are relatively steep, showing the characteristics of steepness in the northeast and slowness in the southwest, suggesting that the abnormal body is steeply inclined to the southwest. The corresponding high positive anomaly of the IV mining area has an irregular ellipse shape, with long axis in east-west direction, about 1000 m long, 850 m wide, and an area of about 0.75 km². Combined with the geological map and the characteristics of physical parameters of rocks and ores, the high positive aeromagnetic anomaly in the mining area is mainly caused by the ore bearing ultrabasic rocks, so the high positive aeromagnetic anomaly is an important indicator of ultrabasic rocks.

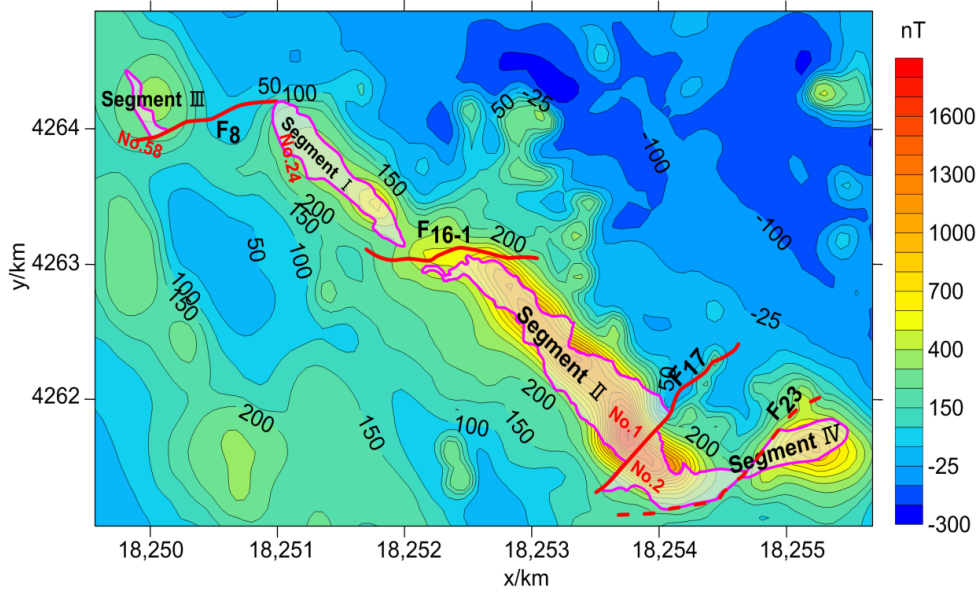


Figure 3. Aeromagnetic anomaly map of the Jinchuan Cu–Ni sulfide deposit after reduction to the pole.

In order to understand the scope of deep ore-bearing rock masses in the mining area, we use the boundary enhancement method presented by Zhang et al. [44] to detect the boundaries of aeromagnetic anomaly in the mining area. It can be seen from the results that the scope of the boundaries of the underground rock masses is determined (Figure 4), especially the edge positions of the deep rock masses of the four mining areas completely covered by the Quaternary are delineated, which provides the exploration scope for the prospecting of the deep Cu–Ni deposit. In order to better understand the characteristics of the deep rock anomalies, we first introduce the dual-tree complex wavelet into the multi-scale anomaly separation of aeromagnetic anomalies. The dual-tree complex wavelet not only has the advantages of wavelet transformation but also the characteristics of approximate translation invariance, more directional selectivity, and limited data redundancy. The results show that with the increase of decomposition scale, the detail information in the shallow part decreases gradually (Figure 5). The range of the high normal anomaly in the second mining area in the southwest side is gradually expanding, indicating that with the increase of burial depth, the range of ore bearing ultrabasic rock masses is gradually expanding, which shows that the deep mining area has a good prospecting potential.

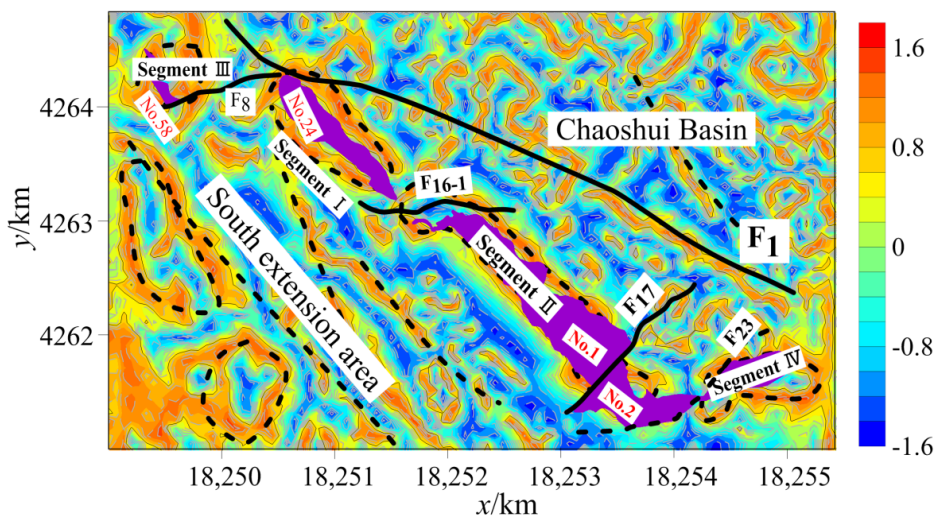


Figure 4. Boundaries detection results of aeromagnetic anomalies in Figure 3.

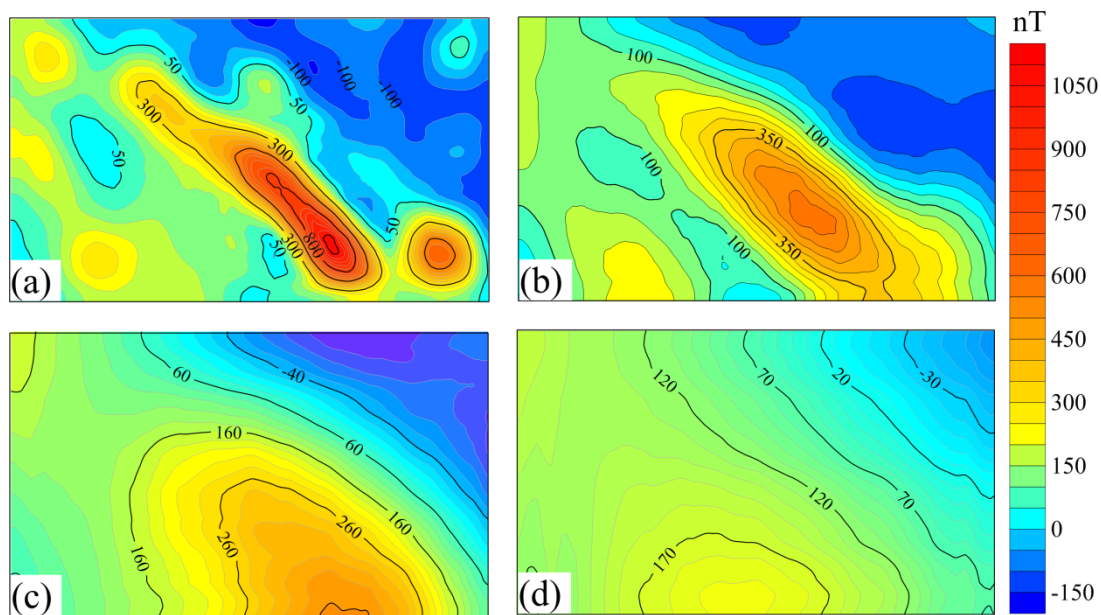


Figure 5. Multiscale separation results (a–d) of the aeromagnetic anomaly in Figure 3 using a dual-tree complex wavelet.

On this basis, we use the gravity and CSAMT data to acquire the locations of the deep potential ore-bearing rock masses in the II and IV mining areas, and the locations of the survey lines are shown in Figure 6. The profiles of gravity and CSAMT data are designed according to the characteristics of magnetic anomalies and the structure of the mining area. The direction of profile Lmg1~3 is 38.38° and that of Lmg4 is 0° . The parameters of CSAMT measurement of the four profiles are determined according to the proposed exploration depth. The minimum receiving and transmitting distance is 12 km, and the maximum is about 16 km. The power supply electrodes are arranged parallel to the survey line, the electrodes distance is 2 km, and the azimuth error is less than 3° . The sampling frequency is 1–9600 Hz, and there are 41 sampling frequency points. The station distance is 50 m. The quality inspection of the CSAMT measurement adopts the method of data observation on the inspection point again. The data quality evaluation is to calculate the mean square relative error of the resistivity of the inspection point. The mean square relative error of the resistivity of the single point in this work is 1.3–4.9%, which meets the specification and design requirements of less than or equal to 5%. The scale of gravity profile (Lmg-1 and 4) work is 1:5000, and the distance between profile points is 20 m. The instrument used is a CG-5 high-precision gravimeter with a reading resolution of $1 \mu\text{gal}$. Before field operation, in addition to various checks and adjustments, static and dynamic tests are carried out to ensure the good performance of the gravimeter in use. The total mean square error of the Bouguer gravity anomaly is $\pm 0.079 \times 10^5 \text{ m/s}^2$, which meets the design requirements and has reliable quality.

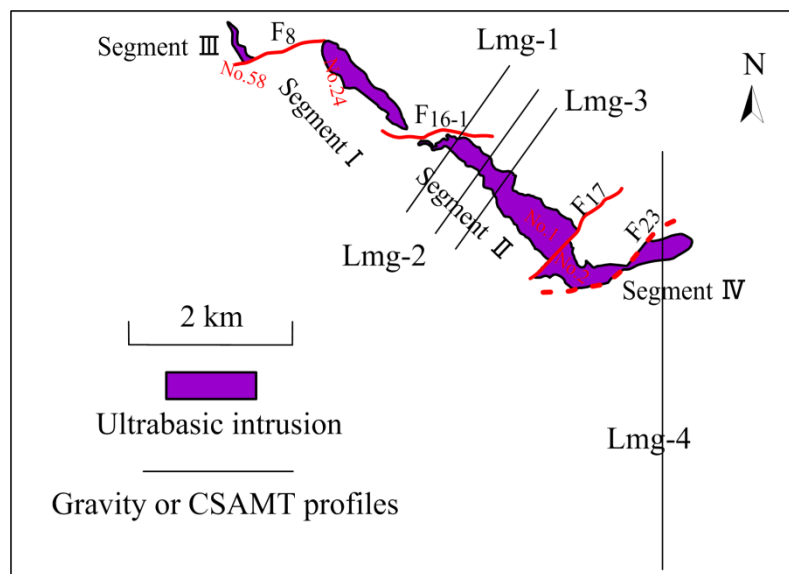


Figure 6. Locations of controlled source audio-frequency magnetotellurics (CSAMT) or gravity exploration lines in the study area.

4. Inversion Methods

In this part, the section gravity, corresponding aeromagnetic data and CSAMT data are inverted to understand the distribution of different geological bodies in the depth of the second and fourth mining areas, so as to predict the favorable prospecting prospect combining with geological data. In this paper, the constraint inversion method based on the SL0 norm tight support is used to process the section gravity and aeromagnetic data.

The following is the principle of tightly supported focused inversion based on the SL0 norm.

If \mathbf{m} is model space and \mathbf{d} is data space, the relationship between the two is \mathbf{F} , and the forward process is expressed as:

$$\mathbf{d} = \mathbf{Fm} \tag{1}$$

The inversion is expressed as:

$$\mathbf{m} = \mathbf{F}^{-1}\mathbf{d} \tag{2}$$

Potential field data inversion is an underdetermined problem. In order to reduce multiple solutions, the Tikhonov regularization method is commonly used. The inversion process can be written as:

$$P^\alpha(\mathbf{m}) = \varphi(\mathbf{m}) + as(\mathbf{m}) \tag{3}$$

Among them, $\varphi(\mathbf{m})$ is the two norm of the difference between the observed data and the theoretical forward data, α is the regularization parameter, $s(\mathbf{m})$ is the stabilizer, which represents the model objective function based on the prior information constraint. In this paper, the minimum compactly supported functional is used as the stabilizer, which can make the inversion result have a better focusing effect [45].

The integral equation is used to express the minimum support functional stabilizers as follows:

$$s_{MS}(\mathbf{m}) = \left\{ \frac{\mathbf{m} - \mathbf{m}_{apr}}{\left[(\mathbf{m} - \mathbf{m}_{apr})^2 + e^2 \right]^{\frac{1}{2}}}, \frac{\mathbf{m} - \mathbf{m}_{apr}}{\left[(\mathbf{m} - \mathbf{m}_{apr})^2 + e^2 \right]^{\frac{1}{2}}} \right\} = \min \tag{4}$$

Among them, $\{a, b\}$ represents the internal product of a and b , which is the focusing factor, and e is the focus factor, which is related to the focus effect of the inversion output. \mathbf{m}_{apr} is a model based on prior information.

To simplify the above formula, variable weight functional $\omega_e(\mathbf{m})$ is introduced, which is expressed as follows:

$$\omega_e(\mathbf{m}) = \frac{1}{\left[(\mathbf{m} - \mathbf{m}_{apr})^2 + e^2 \right]^{\frac{1}{2}}} \tag{5}$$

Equation (4) can be changed to:

$$s_{MS}(\mathbf{m}) = \left\{ \omega_e(\mathbf{m})(\mathbf{m} - \mathbf{m}_{apr}), \omega_e(\mathbf{m})(\mathbf{m} - \mathbf{m}_{apr}) \right\} = \|\mathbf{m} - \mathbf{m}_{apr}\|_{\omega_e}^2 \tag{6}$$

Then, the objective function can be written as:

$$\begin{aligned} P^\alpha(\mathbf{m}, \mathbf{d}) &= \|\mathbf{W}_d \mathbf{A}(\mathbf{m}) - \mathbf{W}_d \mathbf{d}\|^2 + \alpha \|\mathbf{W}_m \mathbf{m} - \mathbf{W}_m \mathbf{m}_{apr}\|_{\omega_e}^2 \\ &= (\mathbf{W}_d \mathbf{A}(\mathbf{m}) - \mathbf{W}_d \mathbf{d})^T (\mathbf{W}_d \mathbf{A}(\mathbf{m}) - \mathbf{W}_d \mathbf{d}) + \alpha (\mathbf{W}_e \mathbf{W}_m \mathbf{m} - \mathbf{W}_e \mathbf{W}_m \mathbf{m}_{apr})^T (\mathbf{W}_e \mathbf{W}_m \mathbf{m} - \mathbf{W}_e \mathbf{W}_m \mathbf{m}_{apr}) \end{aligned} \tag{7}$$

where $\|\mathbf{W}_d \mathbf{A}(\mathbf{m}) - \mathbf{W}_d \mathbf{d}\|^2$ is the fitting difference, $\|\mathbf{W}_m \mathbf{m} - \mathbf{W}_m \mathbf{m}_{apr}\|_{\omega_e}^2$ is the stabilizer, \mathbf{W}_e is the change matrix, which depends on \mathbf{m} , \mathbf{W}_d and \mathbf{W}_m are the weighting matrix of the traditional data space and the model space, respectively. In this paper, \mathbf{W}_d and \mathbf{W}_m are, respectively, as follows:

$$\mathbf{W}_m = \text{diag}(\mathbf{A}^T \mathbf{A})^{1/2} \tag{8}$$

$$\mathbf{W}_d = \text{diag}(\mathbf{A} \mathbf{A}^T)^{1/2} \tag{9}$$

The objective function given by Equation (7) is similar to the traditional objective function form. The difference is that a variable weight matrix needs to be introduced into the model parameters of Equation (7). This paper uses the conjugate gradient method to solve the problem of parameter functional minimization given by Equation (7). In Equation (5), $\omega_e(\mathbf{m})$ can be regarded as a regularization parameter α , and since it also has a focusing effect, it can be called a regularization-focusing factor. As this parameter becomes smaller, the corresponding stabilizer can minimize the non-zero deviation of the model parameters from the prior information.

The smooth L0 algorithm (SL0 algorithm) comes from the sparse signal recovery theory and is used to solve the problem of how to accurately solve \mathbf{m} in the inverse problem. It uses a suitable smooth continuous function to approximate the discontinuous L0 norm and minimizes it by using a minimization algorithm on the smooth function, thereby obtaining the minimum L0 norm and obtaining a sparse solution. In this paper, a Gaussian function with an expected value of 0 is selected to approximate the smooth function of the L0 norm. The continuous function be expressed as:

$$f_\sigma(m) = \frac{\sigma^2}{(m^2 + \sigma^2)} \tag{10}$$

Among them, σ represents the approximate degree of continuous and discontinuous L0 norm. Then there are:

$$\lim_{\sigma \rightarrow 0} f_\sigma(m) = \begin{cases} 1, m = 0 \\ 0, m \neq 0 \end{cases} \tag{11}$$

Or approximately:

$$f_\sigma(m) \approx \begin{cases} 1, |m| \ll \sigma \\ 0, |m| \gg \sigma \end{cases} \tag{12}$$

Define a new function:

$$E_{\sigma}(m) = \sum_{i=1}^M f_{\sigma}(m_i) \quad (13)$$

Then:

$$\lim_{\sigma \rightarrow 0} E_{\sigma}(m) = M - \|m\|_0 \quad (14)$$

The above formula shows that $\|m\|_0 \approx M - F_{\sigma}$ is true when σ is small, and, when $\sigma \rightarrow 0$, this approximate relationship tends to be equal. Therefore, in order to find the solution with the smallest L0 norm, we can take a small value of σ , and make $F_{\sigma}(m)$ the maximum. For small values of σ , F_{σ} is highly uneven and contains many local maxima, so it is difficult to maximize it. For a large value of σ , F_{σ} is smooth and contains fewer local maxima, so it is easier to maximize it. In order to have the largest F_{σ} for any value of σ , this paper uses a decreasing sequence of σ to maximize F_{σ} . For each σ with a large front value, the initial value of the maximization algorithm of F_{σ} is the maximum value of the corresponding F_{σ} . When σ gradually decreases, the initial value of F_{σ} corresponding to each σ starts from the maximum value close to the actual F_{σ} . Therefore, the SL0 algorithm does not fall into the local maximum problem and can find the actual maximum value of F_{σ} for a small value of σ , and give the solution of the smallest L0 norm. Compared with a tightly-supported focused inversion, SL0 norm-constrained tightly-supported focused inversion continuously adjusts \mathbf{W}_e based on a priori information in the form of a weighting function, making the inversion results more accessible to actual physical parameter models.

Therefore, the objective function of the inversion method based on SL0 norm tight support focus can be expressed as follows:

$$\begin{aligned} P_{SL0}^{\alpha}(\mathbf{m}, \mathbf{d}) &= \|\mathbf{W}_d \mathbf{A}(\mathbf{m}) - \mathbf{W}_d \mathbf{d}\|^2 + \alpha \|\mathbf{W}_m \mathbf{m} - \mathbf{W}_m \mathbf{m}_{apr}^{SL0}\|_{\omega_e}^2 \\ &= (\mathbf{W}_d \mathbf{A}(\mathbf{m}) - \mathbf{W}_d \mathbf{d})^T (\mathbf{W}_d \mathbf{A}(\mathbf{m}) - \mathbf{W}_d \mathbf{d}) + \alpha (\mathbf{W}_m \mathbf{m} - \mathbf{W}_m \mathbf{m}_{apr}^{SL0})^T (\mathbf{W}_m \mathbf{m} - \mathbf{W}_m \mathbf{m}_{apr}^{SL0}) \end{aligned} \quad (15)$$

For the CSAMT data, this paper uses the widely used conventional SCS2D software for inversion. This program is an active audio magnetotelluric data processing program developed on the basis of magnetotelluric data processing. Its development level is relatively mature. The suitability selection of SCS2D software inversion parameters is an important part of data processing. The correct selection of inversion parameters will directly affect the accuracy of subsequent data interpretation. The initial background model selected in this paper is a moving average model.

5. Inversion Results and Interpretation

In this section, the section aeromagnetic and gravity data of the II and IV mining areas are inverted based on the SL0 tight support focus inversion method. At the same time, combined with the CSAMT inversion results and geological and rocks' physical properties, the corresponding structures of the survey lines are inferred and interpreted, and the favorable positions of deep mineralization are delineated.

5.1. Survey Results of the II Mining Area

The II mining area is located in the southeast of the F₁₆₋₁ fault and the northwest of the No.56 exploration line, with the largest copper–nickel ore body developed in the Jinchuan Cu–Ni deposit. The ore bearing strata are mainly pre-Sinian Baijiazuzi formations. Faults are developed, mainly including three groups of faults in the NW, NE, and nearly EW directions. The ultrabasic rock body is the ore-bearing parent rock. Under the control of the project, the rock body is in the shape of a rock wall, trending to the northwest, inclining to the southwest, with a length of more than 3000 m. the horizontal thickness is shown as thin at both ends and thick in the middle, up to 1550 m. West of line 26 of the mining area, the occurrence of the ore body is relatively steep, plate like and lens like, and is in the form of a completely intrusive contact or mixed gradual intrusive contact with the early lithofacies.

The ore body to the east of line 26 is in lenticular or stratoid shape. For the deep prospecting of the mining area, the previous study shows that the deep part of No.2 ore body in the II mining area has the possibility of a branch compound and a pinch-out reappearance of ore body. The main reason for this is that the extension of No.2 ore body below the 1000 m level is not revealed, and the geological sections of line 28–30 show that the ore body below the 1100 m level has not been pinched out [2]. Based on the multiple geophysical data, this paper investigates the deep of No.1 ore body so as to find out whether there is the possibility of new ore body in the deep.

The three survey lines of Lmg-1–3 arranged in No.1 ore body of the II mining area coincide with the No.8, 12, and 14 exploration lines, respectively, which are close to each other and are arranged in parallel along the southeast direction. It is of great significance for indicating the deep resistivity, density, and magnetic variations in the profiles. Gravity and CSAMT explorations have been carried out along the Lmg-1 line, respectively. Figure 7 shows the inversion results of gravity and corresponding aeromagnetic data by using the SL0 method. The density and magnetism of the media under the line are obviously different. There are two obvious high-density abnormal areas in the profile, which extend to the deep of the southwest part. The high-magnetism abnormal areas correspond to the high-density abnormal areas and show similar changing characteristics towards the deep. The inversion result of CSAMT shows that the high resistivity areas are distributed on both sides of the profile, the medium-low resistivity areas are mainly located in the middle, tend to the southwest, the dip angle changes from steep to slow, and the extension is large, which is consistent with the high density and high magnetic areas in Figure 7 (Figure 8). CSAMT exploration was also carried out along the Lmg-2 and Lmg-3 lines. The resistivity inversion results and the corresponding aeromagnetic anomaly inversion results show similar resistivity and magnetism distribution characteristics to Lmg-1 (Figure 9).

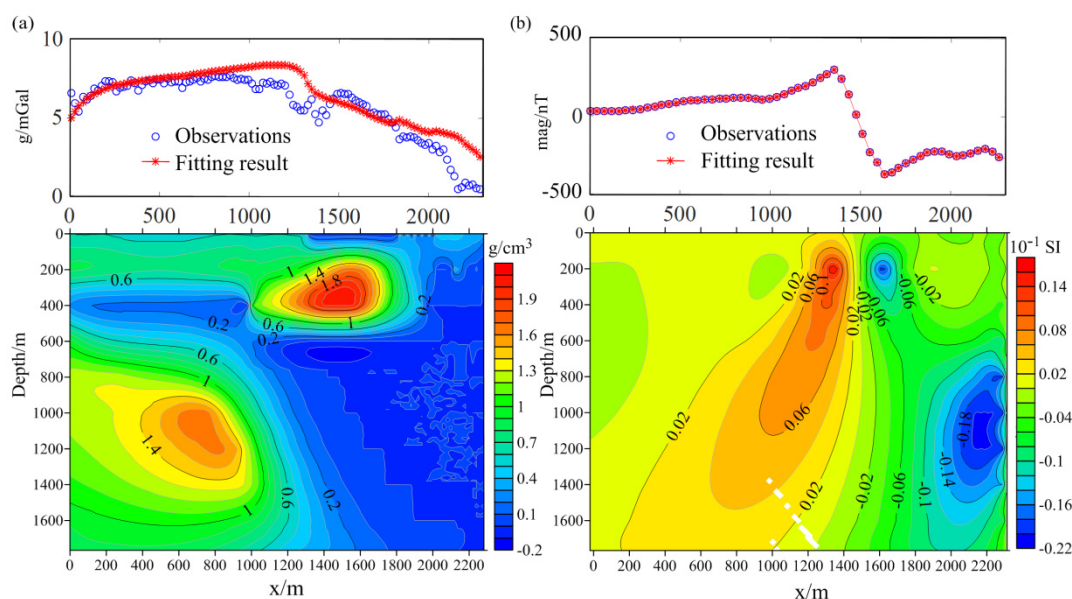


Figure 7. Inversion results of the gravity (a) and aeromagnetic (b) data of Lmg-1.

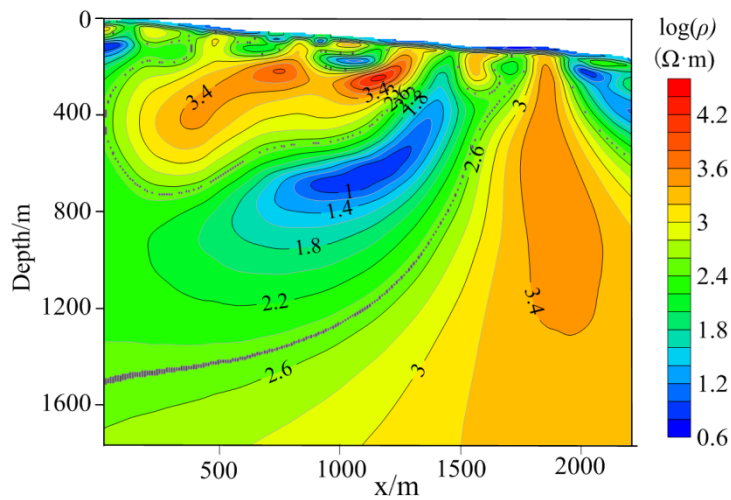


Figure 8. CSAMT data inversion result of the Lmg-1 profile.

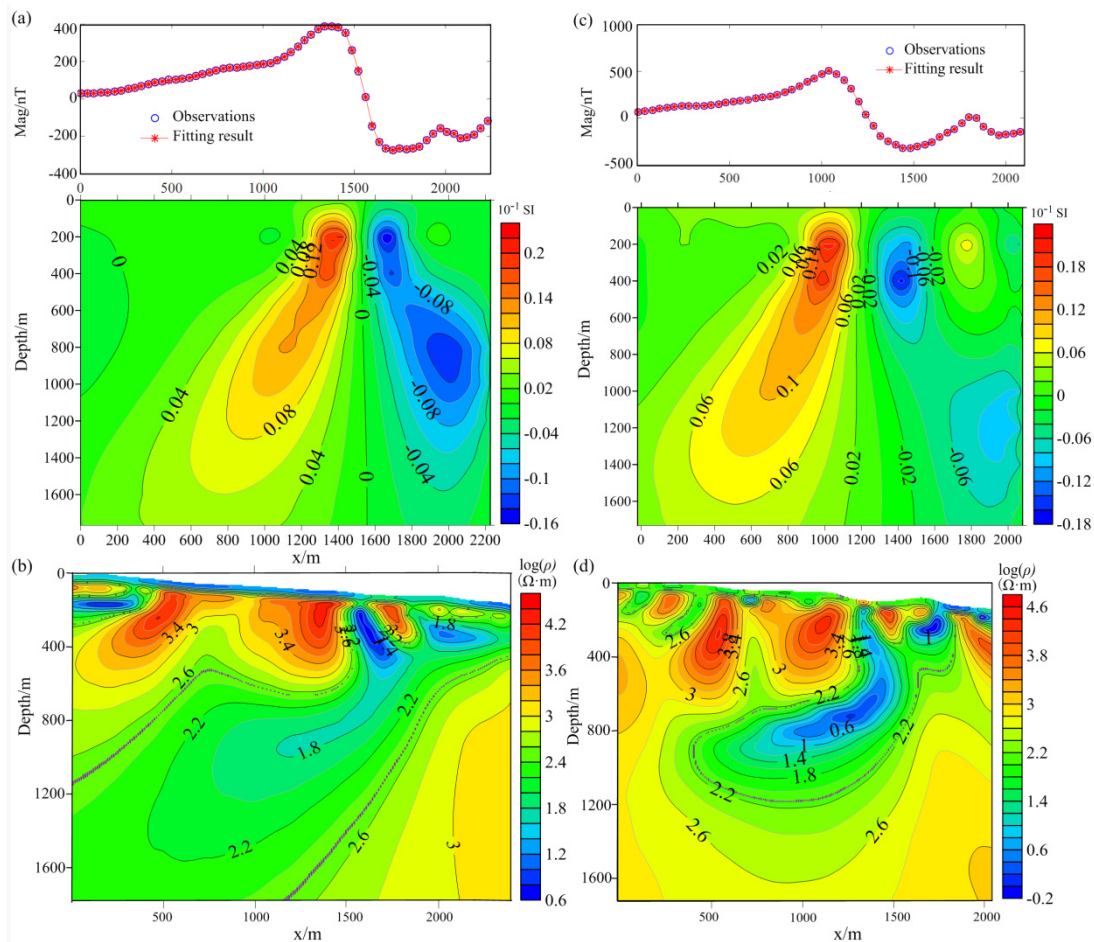


Figure 9. Inversion results of the aeromagnetic (a) and CSAMT (b) data of Lmg-2, and the inversion results of the aeromagnetic (c) and CSAMT (d) data of Lmg-3.

Combined with the geological map, the petrophysical properties of the study area and the results of the known exploration profiles, it is obvious that the high resistivity, low density, and low magnetism areas on both sides of the profiles are caused by the Baijiazuizi formation, the shallow medium-low resistivity, high density, and high magnetism areas are caused by the ore-bearing ultrabasic rock masses, and the transition zone on both sides of the middle abnormal area are the fault zones where ultrabasic rocks intrude into Baijiazuizi formation, as shown by the red dotted line in Figure 10. At the

same time, we can see that the single geophysical method has limitations. For example, the resolution of CSAMT in the deep of the profile is insufficient, and it cannot clearly indicate the location of the deep abnormal target body. Therefore, we have roughly determined the target locations based on the high-density, high-magnetism, medium-low-resistivity geophysical exploration model, and the metallogenic law that is easy to form ore at a low-lying structure place, and we have inferred that the favorable metallogenic location of the line Lmg-1 is about 400–900 m and the burial depth is about 1100–1500 m, the favorable metallogenic area of the line Lmg-2 is about 800–1300 m and the burial depth is about 1200–1700 m, and the favorable metallogenic area of the line Lmg-3 is about 500–1000 m and the burial depth is about 1000–1500 m. The approximate location of the target body is shown by the black dotted line in Figure 10, and three drilling verification locations are designed.

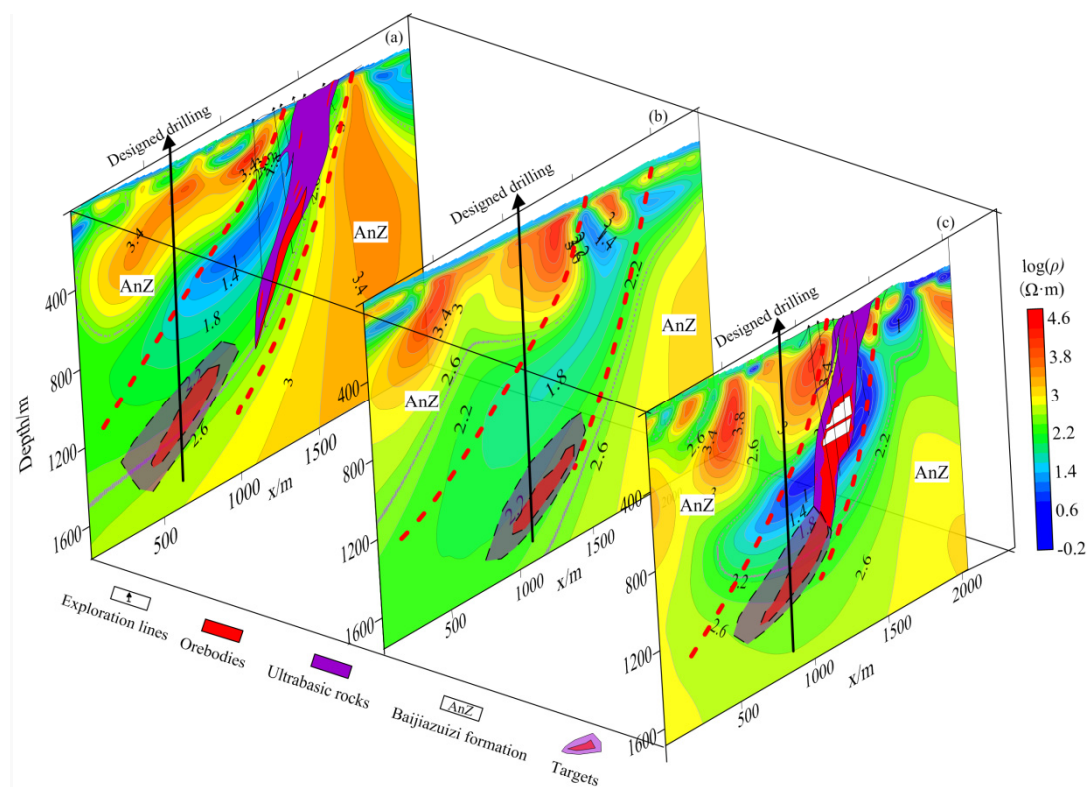


Figure 10. Interpretation results of gravity, aeromagnetic, and CSAMT data and the prediction of deep targets; the targets were indirectly determined based on the inferred locations of the ultrabasic rocks. (a) Lmg-1; (b) Lmg-2; (c) Lmg-3.

5.2. Survey Results of the IV Mining Area

The known ultramafic rock mass in the fourth mining area is 1160 m long and completely covered by the Quaternary. The thickness of the cover layer is 60–140 m. The Bajjiazuizi formation and ore-bearing ultrabasic rock mass are developed below the cover layer. The ore body is dominated by low grade ore, and No.1 ore body is the main ore body. It is produced in the concave section of the bottom of the rock body and is lenticular. The upper and lower parts are small and the middle is large. The strike of the Lmg-4 exploration line in the mining area is just south, passing through No.1 ore body, close to the No.10 exploration line. Gravity and CSAMT surveys were carried out along this line, their lengths are slightly different.

Figure 11 is the inversion results of gravity and aeromagnetic anomalies based on the SL0 algorithm. The corresponding positions in the middle and lower parts of the profile have obvious large high-density and high-magnetic anomaly areas, and they all have the characteristics of extending to the upper left. The inversion result of CSAMT shows that the resistivity on the right side of the

profile is relatively high, the resistivity in the middle is relatively low, and that their contact zone changes from steep to slow towards the deep (Figure 12). Compared with the inversion results in Figure 11, it was found that the high-density and high-magnetic area is consistent with the middle medium-low resistivity area. The inversion results are interpreted in combination with a geological map, the results of a nearby geological exploration line, and the physical parameters of the rocks. It can be seen that the shallow low-density, low-magnetic and low-resistivity areas of the profile are mainly caused by the Quaternary, while the high-resistivity area on the right side is the reflection of Baijiazuzi formation, the high-density, high-magnetic, and low-resistivity area in the upper part of the contact zone corresponds to the known ore-bearing ultrabasic rocks in the four mining areas. At the same time, it is inferred that the transition zone is a fault zone (red dotted line on the right side of Figure 12), which is the channel for ultrabasic magma to intrude into Baijiazuzi formation. Based on the geophysical prospecting model and metallogenic law, we speculate that the deep high density, high magnetism, and medium-low resistivity area in a large range near the channel is the favorable target area for prospecting, and the location is roughly within the survey line 2600–3200 m and its buried depth is 1200–1700 m. At the same time, the drilling hole location is designed, as shown in Figure 12.

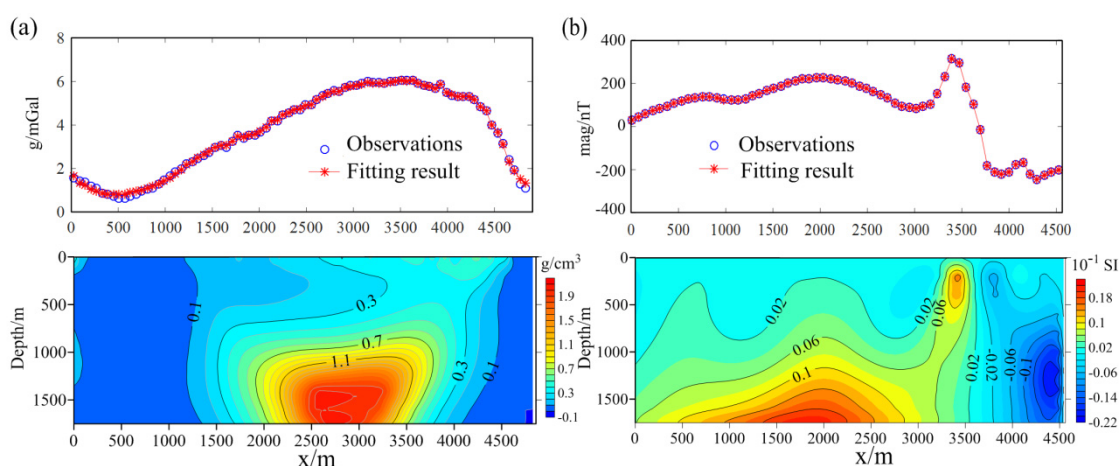


Figure 11. Inversion results of the gravity (a) and aeromagnetic (b) data of Lmg-4.

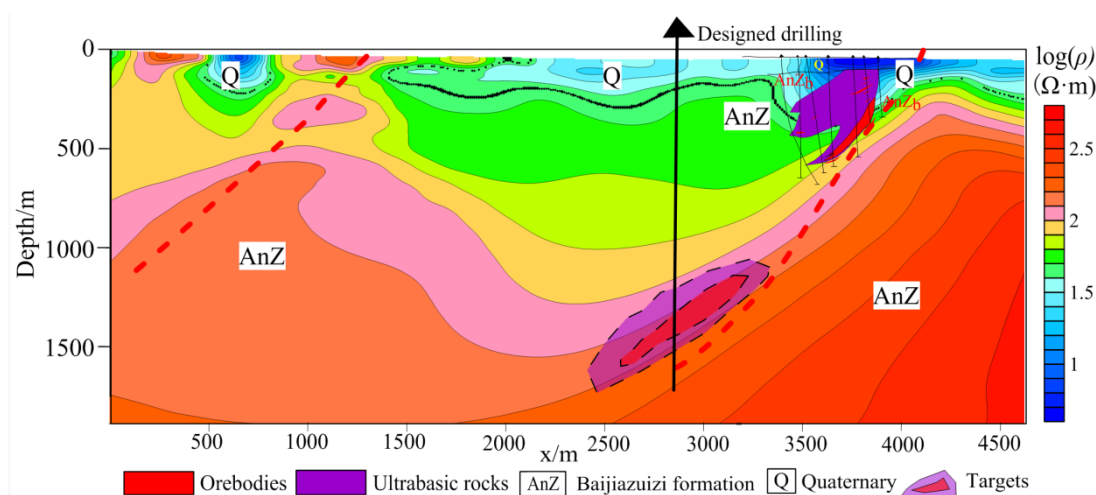


Figure 12. CSAMT data inversion result and interpretation of Lmg-4.

6. Discussion and Conclusions

The geophysical method is an important supporting technology for the exploration of deep metal mineral resources. In this paper, the deep exploration of the Jinchuan Cu–Ni sulfide deposit is carried

out based on the gravity, aeromagnetic, and CSAMT methods with a complementary resolution. Among them, to overcome the ill-posed problem of inversion and reduce the multiplicity of solutions, the focus inversion method based on the SL0 norm is introduced to the inversion of gravity and aeromagnetic data, and the widely used SCS2D inversion software is used for the inversion of CSAMT data, both of which have achieved good inversion results. The medium-low resistivity, high density, and high magnetic areas shown in the inversion results can correspond to the known ore-bearing rocks in the shallow part well. In addition, four favorable target areas are delineated in the deep part of the mining area.

However, these methods are indirect and have some limitations. Because the ultrabasic rock is the parent rock and the surrounding rock of the ore body, the density and magnetism of the two are similar, and the ore body is often located in the middle or lower part of the ultrabasic rock body, so the geophysical signal produced by the ore body is easy to be covered by the ultrabasic rock body, meaning that it is difficult to distinguish the ultrabasic rock body and the ore body. Therefore, more geological data are needed to increase the reliability of target area prediction. In addition, the geophysical data in this paper are limited. It is expected to carry out seismic exploration in the study area and to obtain the velocity structure in the deep part of the mining area, so as to further supplement the supporting evidence of favorable prospective areas. At the same time, it is expected to carry out drilling work at the predicted favorable prospective areas, so as to further verify the results of geophysical deep exploration in this paper.

In general, it is of great significance to study the deep exploration of the Cu–Ni deposit in Jinchuan based on multiple geophysical methods. CSAMT, gravity, and aeromagnetic data not only indicate the known ore locations of the II and IV mining areas but also indicate the favorable ore locations in the deep. At the same time, this achievement provides a good reference for further deep exploration of the mining area and its surrounding areas, as well as a good demonstration of the feasibility and effectiveness of the geophysical methods used to detect deep metal mines.

Author Contributions: Conceptualization, Z.Z.; Methodology, Z.Z. and J.Z.; data curation, Z.Z. and J.Z.; software, X.Z.; validation, Z.Z., X.Z. and M.G.; formal analysis, J.L. and Y.Z.; writing—original draft preparation, J.Z.; writing—review & editing, Z.Z. and J.L.; project administration, Z.Z.; funding acquisition, Z.Z. and J.L. All authors have read and agreed to the published version of the manuscript.

Funding: This work is supported by the National Key Research and Development Program of China (2016YFC0600505), the National Natural Science Foundation of China (41874134) and Jilin Excellent Youth Fund (20190103142JH).

Acknowledgments: We would like to thank the editor and reviewers for their reviews that improved the content of this paper, and thank the Jinchuan Group Co., Ltd. for the providing of geological and geophysical data.

Conflicts of Interest: The authors declare no conflict of interest.

References

1. Teng, J.; Liu, J.; Liu, C.; Yao, J.; Han, L.; Zhang, Y. Prospecting for metal ore deposits in second deep space of crustal interior, the building of strategy reserve base of northeast China. *J. Jilin Univ. (Earth Sci. Ed.)* **2007**, *37*, 633–651.
2. Gao, Y. Study on Geological Characteristics, Temporal and Spatial Evolution, Prospecting in the Depth and Border of Jinchuan Deposit. Ph.D. Thesis, Lanzhou University, Lanzhou, China, 2009.
3. Song, X.; Hu, R.; Chen, L. Characteristics and inspirations of the Ni-Cu sulfide deposits in China. *J. Nanjing Univ. (Nat. Sci.)* **2018**, *54*, 221–235.
4. Wei, Z. Analysis on the Genetic Type and Metallogenic Prognosis about Orebody No. 58 of Jinchuan Copper–Nickel Deposit, Gansu Province. Master’s Thesis, Central South University, Changsha, China, 2009.
5. Li, J.; Hanafy, S.; Schuster, G. Dispersion inversion of guided P-waves in a waveguide of arbitrary geometry. *J. Geophys. Res. Solid Earth* **2018**, *123*, 7760–7774. [[CrossRef](#)]
6. Zeng, Z.; Zhao, X.; Li, Z.; Li, J.; Wang, K.; Ma, L. Geophysical characteristics of the Shuanghu District in the Lungmu Co-Shuanghu-Lancangriver suture zone. *Chin. J. Geophys.* **2016**, *59*, 4594–4602.

7. Zeng, Z.; Huai, N.; Li, J.; Zhao, Z.; Liu, C.; Hu, Y.; Zhang, L.; Hu, Z.; Yang, H. Stochastic inversion of cross-borehole radar data from metalliferous vein detection. *J. Geophys. Eng.* **2017**, *14*, 1327. [[CrossRef](#)]
8. Li, J.; Sun, Z.; Weng, A.; Fan, Q. Determination of metallogenic tectonic environment by rock resistivity value—with Xia Dian Gold deposit as example. *Gold* **2008**, *29*, 15–19. (In Chinese)
9. Thmos, M.D.; Ford, K.L.; Keating, P. Review paper: Exploration geophysics for intrusion-hosted rare metals. *Geophys. Prospect.* **2016**, *64*, 1275–1304. [[CrossRef](#)]
10. Zhao, Z.; Zhou, X.; Guo, N.; Zhang, H.; Liu, Z.; Zheng, Y.; Zeng, Z.; Chen, Y. Superimposed W and Ag-Pb-Zn (-Cu-Au) mineralization and deep prospecting: Insight from a geophysical investigation of the Yinkeng orefield, South China. *Ore Geol. Rev.* **2018**, *93*, 404–412. [[CrossRef](#)]
11. Kheyrollahi, H.; Alinia, F.; Ghods, A. Regional magnetic lithologies and structures as controls on porphyry copper deposits: Evidence from Iran. *Explor. Geophys.* **2016**, *49*, 98–110. [[CrossRef](#)]
12. Xiao, F.; Wang, Z. Geological interpretation of Bouguer gravity and aeromagnetic data from the Gobi-desert covered area, Eastern Tianshan, China: Implications for porphyry Cu-Mo polymetallic deposits exploration. *Ore Geol. Rev.* **2017**, *80*, 1042–1055. [[CrossRef](#)]
13. Hu, X.; Peng, R.; Wu, G.; Wang, W.; Huo, G.; Han, B. Mineral exploration using CSAMT data: Application to Longmen region metallogenic belt, Guangdong Province, China. *Geophysics* **2013**, *78*, B111–B119. [[CrossRef](#)]
14. Guo, Z.; Hu, L.; Liu, C.; Cao, C.; Liu, J.; Liu, R. Application of the CSAMT method to Pb–Zn mineral deposits: A case study in Jiashui, China. *Minerals* **2019**, *9*, 726. [[CrossRef](#)]
15. Shah, A.K.; Bedrosian, P.A.; Anderson, E.D.; Kelley, K.D.; Lang, J. Integrated geophysical imaging of a concealed mineral deposit: A case study of the world-class Pebble porphyry deposit in southwestern Alaska. *Geophysics* **2013**, *78*, B317–B328. [[CrossRef](#)]
16. Zhang, R.; Li, T. Joint inversion of 2D gravity gradiometry and magnetotelluric data in mineral exploration. *Minerals* **2019**, *9*, 541. [[CrossRef](#)]
17. Melo, A.T.; Sun, J.; Li, Y. Geophysical inversions applied to 3D geology characterization of an iron oxide copper-gold deposit in Brazil. *Geophysics* **2017**, *82*, K1–K13. [[CrossRef](#)]
18. Lee, B.M.; Unsworth, M.J.; Hübert, J.; Richards, J.P.; Legault, J.M. 3D joint inversion of magnetotelluric and airborne tipper data: A casestudy from the Morrison porphyry Cu–Au–Mo deposit, British Columbia, Canada. *Geophys. Prospect.* **2018**, *66*, 397–421. [[CrossRef](#)]
19. Zhang, X.; Zhao, X.; Xie, Z. The application of the gravity and magnetic method to the exploration of the eastward extending M-15 anomaly of the Jinchuan copper–nickel deposit. *Geophys. Geochem. Explor.* **2010**, *34*, 139–143.
20. Wen, M.; Luo, X. A study of the ore-prospecting work based on multiple geosciences information in the Jinchuan Cu–Ni deposit. *Geol. China* **2013**, *40*, 594–601.
21. Fu, K.; Li, B. Geological and geophysical composite exploration model of Jinchuan copper–nickel sulfide deposit in Gansu province. *Gansu Geol.* **2006**, *15*, 62–67.
22. Tang, Z.L.; Li, W.Y. *Mineralisation Model and Geology of the Jinchuan Ni–Cu Sulfide Deposit Bearing PGE*; Geological Publishing House: Beijing, China, 1995. (In Chinese)
23. Song, X.; Danyushevsky, L.V.; Keays, R.R.; Chen, L.; Wang, Y.; Tian, Y.; Xiao, J. Structural, lithological, and geochemical constraints on the dynamic magma plumbing system of the Jinchuan Ni-Cu sulfide deposit, NW China. *Min. Depos.* **2012**, *47*, 277–297. [[CrossRef](#)]
24. Zhao, G.; Cawood, P.A. Precambrian geology of China. *Precamb. Res.* **2012**, *222–223*, 13–54. [[CrossRef](#)]
25. Zhao, G.C.; Sun, M.; Wilde, S.A.; Li, S.Z. Late Archean to Paleoproterozoic evolution of the North China Craton: Key issues revisited. *Precamb. Res.* **2005**, *136*, 177–202. [[CrossRef](#)]
26. Zhai, M.G.; Santosh, M. The early Precambrian odyssey of the North China Craton: A synoptic overview. *Gondwana Res.* **2011**, *20*, 6–25. [[CrossRef](#)]
27. Song, X.Y.; Keays, R.R.; Zhou, M.F.; Qi, L.; Ihlenfeld, C.; Xiao, J.F. Siderophile and chalcophile elemental constraints on the origin of the Jinchuan Ni-Cu-(PGE) sulfide deposit, NW China. *Geochim. Cosmochim. Acta* **2009**, *73*, 404–424. [[CrossRef](#)]
28. Mao, X.; Li, L.; Liu, Z.; Zeng, R.; Dick, J.M.; Yue, B.; Ai, Q. Multiple Magma Conduits Model of the Jinchuan Ni-Cu-(PGE) Deposit, Northwestern China: Constraints from the Geochemistry of Platinum-Group Elements. *Minerals* **2019**, *9*, 187. [[CrossRef](#)]
29. Xu, A.D.; Jiang, X.D. Characteristics and geological significance of the Dunzigou Group of the mesoproterozoic in the western edge of the North China Platform. *J. Earth Sci. Environ.* **2003**, *25*, 27–31. (In Chinese)

30. Xiao, P.X.; You, W.F.; Cao, X.D. Redefining of the Hanmushan Group in Longshoushan, central-western Gansu Province. *Geol. Bull. China* **2011**, *30*, 1228–1232. (In Chinese)
31. Xie, C.R.; Xiao, P.X.; Yang, Z.Z.; Cao, X.D.; Hu, Y.X. Progress in the studying of the Hanmushan Group in the Longshou mountains of Gansu province. *J. Stratigr.* **2013**, *37*, 54–57. (In Chinese)
32. Barnes, S.J.; Naldrett, A.J.; Gorton, M.P. The origin of the fractionation of platinum-group elements in terrestrial magmas. *Chem. Geol.* **1985**, *53*, 303–323. [[CrossRef](#)]
33. Tung, K.A.; Yang, H.Y.; Liu, D.Y.; Zhang, J.X.; Tseng, C.Y.; Wan, Y.S. SHRIMP U–Pb geochronology of the detrital zircons from the Longshoushan Group and its tectonic significance. *Chin. Sci. Bull.* **2007**, *52*, 1414–1425. [[CrossRef](#)]
34. Tang, Z.L.; Bai, Y.L. Geotectonic framework and metallogenic system in the southwest margin of north China paleocontinent. *Geosci. Front.* **1999**, *6*, 78–90. (In Chinese)
35. Zeng, R.Y.; Lai, J.Q.; Mao, X.C.; Li, B.; Zhang, J.D.; Bayless, R.; Yang, L.Z. Paleoproterozoic Multiple Tectonothermal Events in the Longshoushan Area, Western North China Craton and Their Geological Implication: Evidence from Geochemistry, Zircon U–Pb Geochronology and Hf Isotopes. *Minerals* **2018**, *8*, 361. [[CrossRef](#)]
36. Gong, J.H.; Zhang, J.X.; Wang, Z.Q.; Yu, S.Y.; Li, H.K.; Li, Y.S. Origin of the Alxa Block, western China: New evidence from zircon U–Pb geochronology and Hf isotopes of the Longshoushan Complex. *Gondwana Res.* **2016**, *36*, 359–375. [[CrossRef](#)]
37. Xiu, Q.Y.; Lu, S.N.; Yu, H.F.; Yang, C.L. The isotopic age evidence for main Longshoushan Group contributing to Palaeoproterozoic. *Prog. Precamb. Res.* **2002**, *25*, 93–96. (In Chinese)
38. Duan, J.; Li, C.S.; Qian, Z.Z.; Jiao, J.G. Geochronological and geochemical constraints on the petrogenesis and tectonic significance of Paleozoic dolerite dykes in the southern margin of Alxa Block, North China Craton. *J. Asian Earth Sci.* **2015**, *111*, 244–253. [[CrossRef](#)]
39. Zeng, R.Y.; Lai, J.Q.; Mao, X.C.; Li, B.; Ju, P.J.; Tao, S.L. Geochemistry, zircon U–Pb dating and Hf isotopies composition of Paleozoic granitoids in Jinchuan, NW China: Constraints on their petrogenesis, source characteristics and tectonic implication. *J. Asian Earth Sci.* **2016**, *121*, 20–33. [[CrossRef](#)]
40. Li, X.H.; Su, L.; Chung, S.L.; Li, Z.X.; Liu, Y.; Song, B.; Liu, D.Y. Formation of the Jinchuan ultramafic intrusion and the world's third largest Ni–Cu sulfide deposit: Associated with the ~825 Ma south China mantle plume? *Geochem. Geophys. Geosyst.* **2005**, *6*, 1–16. [[CrossRef](#)]
41. Zhang, M.J.; Kamo, S.L.; Li, C.S.; Hu, P.Q.; Ripley, E.M. Precise U–Pb zircon-baddeleyite age of the Jinchuan sulfide ore-bearing ultramafic intrusion, western China. *Miner. Depos.* **2010**, *45*, 3–9. [[CrossRef](#)]
42. Jiang, J.J.; Chen, L.M.; Song, X.Y.; Fu, Z.Q.; Wang, L.; Lu, J.Q.; Ai, Q.X.; Li, H. Siderophile and chalcophile element geochemistry of No. 58 ore body in Jinchuan Cu–Ni sulfide deposit and its geological significance. *Miner. Depos.* **2013**, *32*, 941–953. (In Chinese)
43. Li, T.H.; Luo, X.R.; Peng, Q.L.; Wang, W.; Luo, X.P.; Song, Z.B.; Wen, X.Q. Geological-geochemical-geophysical multifactor information ore prognosis in the depth and on the edge of No.1 mining area of the Jinchuan copper–nickel sulfide ore deposit, Gansu Province. *Geol. Bull. China* **2012**, *31*, 1192–1200. (In Chinese)
44. Zhang, J.M.; Zeng, Z.F.; Wu, Y.G.; Du, W.; Wang, Y.Z. Balanced morphological filters for horizontal boundaries enhancement of the potential field sources. *Appl. Geophys.* **2020**, 1–10. [[CrossRef](#)]
45. Zhao, X. The Study and Application on the Gravity and Magnetic Joint Inversion Based on the Smoothed L0 Norm (SL0) Constraint of Compactly Supported Conjugate Gradient Algorithm. Master's Thesis, Jilin University, Changchun, China, 2017.

